A multi-scale mechanobiological framework for vibration-induced intimal hyperplasia

Maha Reda[1,2,3*], Jérôme Chambert[2], Emmanuelle Jacquet[2], Nicla Settembre[4], Christophe Noël[1]

[1*]Electromagnetism, Vibration, Optics Laboratory, Institut national de recherche et de sécurité (INRS), 54500, Vandœuvre-lès-Nancy, France.
[2] Université Marie et Louis Pasteur, CNRS, institut FEMTO-ST, F-25000, Besançon, France.
[3]Mines Saint-Étienne, U1059 Sainbiose, INSERM, 42000, Saint-Étienne, France.
[4]Department of Vascular Surgery, Nancy University Hospital, Vandœuvre-lès-Nancy, 54500, France.

*Corresponding author(s). E-mail(s): maha.reda@emse.fr;
Contributing authors: jerome.chambert@univ-fcomte.fr;
emmanuelle.jacquet@univ-fcomte.fr ; nicla.settembre@univ-lorraine.fr;
christophe.noel@inrs.fr;

Abstract

Intimal hyperplasia is a pathological mechanism underlying arterial growth and remodeling in numerous vascular diseases, in which key biological processes are regulated by mechanical fields such as wall shear stress (WSS) and circumferential stress within the artery walls. In the present study, we hypothesize that chronic exposure to hand-arm vibrations (HAV) contributes to the development of intimal hyperplasia in the digital artery through vibration-induced reductions in WSS. Accordingly, a mechanobiological framework coupling an agent-based model (ABM) with a finite element model (FEM) was developed. The ABM captures the hemodynamics-driven and mechanoregulated cellular and molecular mechanisms involved in this pathology, including mediator secretion by endothelial and smooth muscle cells (SMCs), SMCs proliferation and migration, and extracellular matrix (ECM) synthesis and degradation. WSS values, reflecting the presence or absence of vibration during long-term working conditions, were used as model inputs. Circumferential stresses were computed using the FEM,

which describes the mechanical behavior of the digital artery. The model parameters were identified from our experimental findings and literature data. Over a five-year period of vibration exposure (4h/day), our simulations revealed that the constitutive law of the arterial walls had a negligible impact on the progression of stenosis. Moreover, reductions in circumferential stress associated with arterial wall thickening led to ECM degradation in the media layer due to an increase in the production of matrix metalloproteinase-2. This mechanobiological framework provides a computational tool for estimating vibration-induced stenosis rates and can be extended to study intimal hyperplasia in diverse biomechanical and pathological contexts.

Keywords: mechanobiology, intimal hyperplasia, finite element, vibration

1 Introduction

Exposure to hand-arm vibrations (HAVs) can cause an imbalance in some mechanical and hemodynamic fields at the level of the digital arteries (Noël and Settembre 2022; Noël and Settembre 2024; Curry et al. 2002). In a homeostatic state, the balance of these parameters around baseline values allows the artery to function according to its physiological requirements. However, any alteration of the homeostatic state could trigger an adaptive response aimed at restoring the balance of disrupted mechanical parameters and re-establishing vascular homeostasis. In the case of vibration exposure, a long-term exposure to high-level vibration may lead to the development of the vibration-induced Raynaud's syndrome which is a peripheral vascular disorder characterized by arterial stenosis that is partially due to an intimal hyperplasia (Brammer et al. 1987; Okada et al. 1987; Takeuchi et al. 1985). Studies have shown that exposure to vibration reduces Wall Shear Stress (WSS) in digital arteries (Noël and Settembre 2022; Noël and Settembre 2024). WSS plays a key role in arterial growth and remodeling through the regulation of the endothelial functions (Epstein et al. 1994; Nerem et al. 1998). Low WSS stimulates the endothelium to release mitogenic and chemotactic factors, such as Platelet-Derived Growth Factor (PDGF), which promote Smooth Muscle Cell (SMC) proliferation, migration, and extracellular matrix (ECM) remodeling (Hsieh et al. 1991; Minion et al. 2000; Koyama et al. 1994). Similarly, changes in circumferential stress due to arterial growth or remodeling can induce SMC mechanotransduction, further regulating these cellular processes and contributing to vascular remodeling and intimal hyperplasia (Kona et al. 2009; Bayer et al. 1999).

Numerous studies have modeled arterial growth and remodeling in various vascular pathologies, using approaches ranging from continuum models at the macroscopic scale, to mixture models incorporating vascular components, and microscale models such as agent-based models (ABMs). ABMs are particularly suited to capturing individual cell behavior and can be coupled with continuum models at the tissue scale (Corti et al. 2021). Since mechanical stresses regulate cellular mechanisms, finite element models (FEM) are often employed to compute stress fields (e.g., circumferential or Hoop stress, and longitudinal stresses) that can then modulate ABM dynamics.

For instance, (Boyle et al. 2010) modeled restenosis after stent placement using an ABM-FEM coupling, while (Zahedmanesh and Lally 2012) applied a similar framework to vascular tissue engineering, linking cyclic deformations of stents to SMC dynamics. (Corti et al. 2020) investigated atherosclerosis through shear-stress-driven intimal hyperplasia using an ABM coupled to a fluid mechanics model. Multi-scale ABM-FEM models have also been applied to restenosis (Boyle et al. 2010; Nolan and Lally 2018; Tahir et al. 2011; Caiazzo et al. 2011; Li et al. 2019) and to arterial wall growth under hypertension (Keshavarzian et al. 2018), where mechanical fields were explicitly linked to growth factor secretion and SMC proliferation.

Intimal hyperplasia constitutes a multifactorial phenomenon, resulting from intricate interactions between cellular mechanisms and mechanical forces. To investigate these processes, we established a coupled ABM-FEM framework. While only a few studies have addressed arterial remodeling in vibration-induced Raynaud's syndrome (Reda et al. 2022), our approach specifically accounts for the influence of stress fields on cellular behaviors such as growth factor secretion and ECM remodeling. In this framework, the ABM describes biological processes at the cellular and molecular scales, whereas the FEM simulates the arterial mechanical response using hyperelastic constitutive laws. Coupling these models enables the calculation of circumferential stress during growth and its feedback on cellular regulation. This multi-scale, multi-physics framework provides a novel tool to investigate and predict the long-term arterial remodeling associated with chronic vibration exposure in the hand-arm system.

2 Material and methods

This multiscale framework expands upon a previously developed ABM (Reda et al. 2022) based in NetLogo (Wilensky et al. 1999). In this current study, our previous ABM was coupled to an FEM developed in FEniCs, an open source code for finite element analysis (Alnæs et al. 2015). This coupling permits the simulation of updated circumferential stress fields as the arterial geometry evolves within the ABM during the growth process. This stress field, reintroduced into the ABM, then enables the mechanoregulation of biological phenomena (Figure 1). The model was tested under two states: i) the 'No Vibration' state in which no exposure to vibration was simulated and the WSS value was kept to its physiological value during the simulation time ($\tau = 3$ Pa), and ii) the 'Vibration' state in which the physiological WSS value was perturbed by regular drops ($\tau = 1$ Pa) replicating the daily working condition of workers exposed to HAVs (Noël and Settembre 2022; Noël and Settembre 2024).

2.1 Agent-based model

2.1.1 ABM overview

The ABM previously described in (Reda et al. 2022) was designed to capture some of the biological processes involved in vibration-induced intimal hyperplasia. The model was implemented on a 2D lattice representation of a cross-sectional slice of a healthy artery, discretized into square patches of 10 μm $\times$ 10 μm. Each patch could be occupied by a single agent representing one of the three major cellular or extracellular

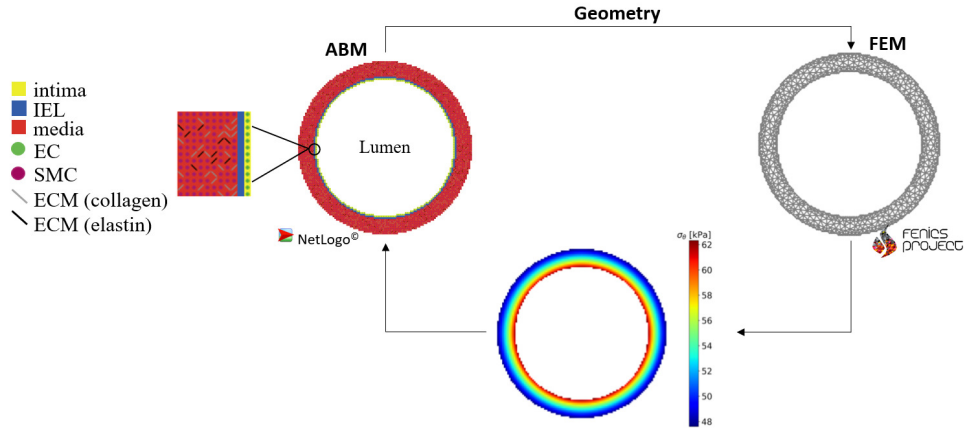

Fig. 1 ABM-FEM coupling scheme. The arterial geometry generated by the ABM is transferred to the FEM to compute circumferential stresses, which are then fed back into the ABM.

components: endothelial cells (ECs), smooth muscle cells (SMCs), or extracellular matrix (ECM) constituents. The intima consisted of a monolayer of ECs, while the media was composed of SMCs and ECM agents (collagen or elastin) in physiologically relevant proportions. Patches were assigned a type (intima, media, lumen, IEL, or boundary) and could update it dynamically to account for geometric changes during arterial remodeling.

2.1.2 Cellular mechanisms modulated by the WSS

Biological mechanisms in the ABM were regulated primarily by WSS. A physiological WSS value of 3 Pa was used to initialize the system, while a drop to 1 Pa was applied to mimic vibration exposure. ECs acted as the primary sensors of WSS and modulated the local microenvironment through the secretion of signaling molecules. In particular, they secreted platelet-derived growth factor (PDGF-BB) and transforming growth factor-beta (TGF-β), which promoted SMC proliferation and ECM remodeling; nitric oxide (NO), which exerted an anti-proliferative effect on SMCs; and matrix metalloproteinases (MMPs), which contributed to ECM degradation. These biochemical cues were implemented as diffusing mediators in the ABM and regulated the probabilistic rules governing SMC and ECM dynamics (i.e., proliferation, migration, apoptosis).

SMC probabilistic behaviors included proliferation, apoptosis, and migration from the media to the intima, all of which were modulated by WSS-induced EC signaling; i.e., the diffused factors secreted by the ECs.

Model parameters, including mediator secretion rates, degradation constants, and SMC behavioral probabilities, were obtained from the literature and further calibrated against our in vitro flow experiments (Reda et al. 2022). These experiments, performed under controlled WSS conditions, provided quantitative data to refine the secretion dynamics of EC-derived growth factor (PDGF-BB), ensuring that the model reproduced physiologically consistent responses to changes in WSS values. All

remaining biological parameters and behavioral rules were derived from experimental and modeling studies reported in the literature. Further details regarding parameter identification and calibration can be found in Appendix A.

2.1.3 Cellular mechanisms modulated by the circumferential stress

SMC secretory rules: Arterial growth and remodeling are not only regulated by WSS but are also strongly influenced by the circumferential stresses generated within the arterial wall. In this study, we incorporated these mechanosensitive mechanisms and summarized below the rules governing SMC secretion of growth factors and ECM remodeling. Studies have shown that SMCs secrete PDGF-BB and TGF-β when exposed to high circumferential stresses, as in the case of hypertension. In our model, these mechanisms were incorporated by an increase in PDGF-BB and TGF-β secretion when circumferential stress (σ_θ) exceeds a threshold, corresponding to the homeostatic stress level (Bayer et al. 1999; Keshavarzian et al. 2018). This threshold was defined as the maximum circumferential stress ($\sigma_{\max}$) observed in the arterial wall under basal conditions. The corresponding secretion rules of PDGF-BB and TGF-β were given by equation (1) and (2) respectively.

$$m^{\text{SMC}}_{\text{PDGF-BB}}(\sigma_\theta) = \begin{cases} 0 & \text{if } \sigma_\theta \leq \sigma_{\max} \\ m_{\text{PDGF-BB}} \times (\sigma_\theta - \sigma_{\max}) & \text{if } \sigma_\theta > \sigma_{\max} \end{cases} \tag{1}$$

$$m^{\text{SMC}}_{\text{TGF-}\beta}(\sigma_\theta) = \begin{cases} 0 & \text{if } \sigma_\theta \leq \sigma_{\max} \\ m_{\text{TGF-}\beta} \times (\sigma_\theta - \sigma_{\max}) & \text{if } \sigma_\theta > \sigma_{\max} \end{cases} \tag{2}$$

where $m^{\text{SMC}}_{\text{PDGF-BB}}(\sigma_\theta)$ and $m^{\text{SMC}}_{\text{TGF-}\beta}(\sigma_\theta)$ are the masses of respectively PDGF-BB and TGF-β both produced by a SMC under stress, as brought up earlier, $\sigma_\theta^{\max}$ denotes the maximum stress value within the healthy artery under basal conditions (basal WSS and blood pressure), worked out from our FEM, thereby depending on the constitutive law applied to the arterial wall. The secretion coefficients were set to $m_{\text{PDGF-BB}} = 7.98 \times 10^{-5}\ [\text{fg} \cdot \text{kPa}^{-1} \cdot \text{h}^{-1}]$ and $m_{\text{TGF-}\beta} = 2.76 \times 10^{-4}\ [\text{fg} \cdot \text{kPa}^{-1} \cdot \text{h}^{-1}]$.

These two growth factors modulate the proliferation rate of SMCs. Hence, the proliferation probability of SMCs was modeled as the sum of: i) the basal proliferation rate, ii) the PDGF-BB-driven rate, and iii) TGF-β-driven proliferation rate. This probability is determined by the total amount of PDGF-BB and TGF-β, which includes the WSS-dependent release of PDGF-BB and TGF-β by ECs, together with the stress-dependent terms $m^{\text{SMC}}_{\text{PDGF-BB}}(\sigma_\theta)$ and $m^{\text{SMC}}_{\text{TGF-}\beta}(\sigma_\theta)$ associated with σ_θ. The exact formulation of the proliferation probability was described in our previous published work explaining in detail our ABM of intimal hyperplasia (Reda et al. 2022). The keystone is that SMCs' proliferation may depend on σ_θ, and is therefore influenced by the accuracy of the constitutive mechanical law in reproducing the actual behavior of arterial walls. The SMCs' probabilities of apoptosis and migration were not affected by σ_θ (Reda et al. 2022).

Similarly, SMCs also secrete MMP-9 in response to elevated circumferential stress. The secretion rule, adapted from (Keshavarzian et al. 2018) and calibrated to our model's $\sigma_{\max}$, is given by:

$$m^{\text{SMC}}_{\text{MMP}-9}(\sigma_\theta) = \begin{cases} 0 & \text{if } \sigma_\theta \leq \sigma_{\max} \\ M_{\text{MMP}-9}(1 - \exp(-((\sigma_\theta - \sigma_\theta^{\max})/\kappa_{\text{MMP}-9}))) & \text{if } \sigma_\theta > \sigma_{\max} \end{cases} \tag{3}$$

where $m^{\text{SMC}}_{\text{MMP}-9}(\sigma_\theta)$ is the mass of MMP-9 produced by a SMC under mechanical stress, $M_{\text{MMP}-9} = 2.118 \times 10^{-4}$ [fg $\cdot$ h^{-1}] and $\kappa_{\text{MMP}-9} = 26$ [kPa].

We modeled MMP-2 secretion in response to unbalanced circumferential stress by generalizing the mathematical formulation proposed by (Keshavarzian et al. 2018) which was related only to an increase in circumferential stress (this formulation matches the case $\sigma_\theta > \sigma_{\max}$ in eq. (4)). Indeed, experimental evidence from (Bayer et al. 1999) indicates that reduced circumferential stress also stimulates MMP-2 secretion by SMCs, leading to medial atrophy characterized by thinning of the media due to collagen and elastin degradation. To capture this dual behavior, we extended the original formulation to include stress-decrease conditions. Specifically, we assumed that the evolution of MMP-2 secretion follows a similar functional form whether stress increases beyond $\sigma_{\max}$ or decreases below $\sigma_{\min}$. The secretion rule implemented in our model is therefore expressed as:

$$m^{\text{SMC}}_{\text{MMP}-2}(\sigma_\theta) = \begin{cases} 0 & \text{if } \sigma_{\min} \leq \sigma_\theta \leq \sigma_{\max} \\ M_{\text{MMP}-2}(1 - \exp(\alpha((\sigma_\theta - \sigma_\theta^{\text{phys}})/\kappa_{\text{MMP}-2}))) & \text{otherwise} \end{cases} \tag{4}$$

where $m^{\text{SMC}}_{\text{MMP}-2}(\sigma_\theta)$ is the mass of MMP-2 secreted by SMC under stress, $\alpha = 1$ and $\sigma_\theta^{\text{phys}} = \sigma_{\min}$ if $\sigma_\theta < \sigma_{\min}$, $\alpha = -1$ and $\sigma_\theta^{\text{phys}} = \sigma_{\max}$ if $\sigma_\theta > \sigma_{\min}$, $M_{\text{MMP}-2} = 7,347 \times 10^{-2}$ [fg$\cdot$h^{-1}] and $\kappa_{\text{MMP}-2} = 56,28$ kPa.

In addition, the natural degradation of MMP-2 was included and set to 1% per hour, consistent with (Zahedmanesh and Lally 2012). The lower stress threshold, $\sigma_{\min}$, corresponds to the minimum value of the circumferential stress field within the healthy arterial wall for basal conditions and, like $\sigma_{\max}$, was computed from our mechanical model based on the chosen constitutive law. These mechanoregulation thresholds ($\sigma_{\min}$ and $\sigma_{\max}$) were interpreted as lower and upper homeostatic circumferential stress limits governing SMC mechanotransduction. Within this physiological stress range, the arterial wall was assumed to remain in a homeostatic state with balanced ECM turnover and limited secretion of remodeling mediators. In contrast, circumferential stress values outside this range were assumed to trigger phenotypic changes in SMCs, leading to altered secretion of growth factors and MMPs involved in arterial remodeling and intimal hyperplasia progression.

Secretion/Degradation of the ECM: The degradation and secretion of the ECM play a crucial role in vascular remodeling and the migration of SMCs (Sakamoto et al. 2006). Indeed, during the process of intimal hyperplasia, the ECM is degraded by the MMPs to facilitate the migration of SMCs from the media to the intima. As

a result, a reorganization of the ECM structure may occur in the media, potentially leading to changes in the mechanical behavior of the artery. The ECM dynamics modulated by the circumferential stress are modeled as probabilities and listed below.

Firstly, the probability of collagen secretion by one SMC modulated by TGF-β is given as follows:

$$\mathcal{S}_{\text{TGF}-\beta}(\sigma_\theta) = \gamma_{\text{TGF}-\beta} \times m^{\text{SMC}}_{\text{TGF}-\beta}(\sigma_\theta) \tag{5}$$

with $m^{\text{SMC}}_{\text{TGF}-\beta}(\sigma_\theta)$ in $[\text{fg}\cdot\text{h}^{-1}]$ is expressed by equation (2) and $\gamma_{\text{TGF}-\beta} = 2,27\times10^{-5}$ fg^{-1}.

Secondly, we modeled the probability of collagen degradation by one SMC modulated by MMP-2:

$${}^{\text{m}}\mathcal{D}^{\text{c}}_{\text{MMP}-2}(\tau,\sigma_\theta) = \gamma_{\text{MMP}-2} \times m_{\text{MMP}-2}(\tau,\sigma_\theta) \tag{6}$$

with $\gamma_{\text{MMP}-2} = 3,5\times10^{-4}$ fg^{-1} and $m_{\text{MMP}-2}(\tau,\sigma_\theta) = m^{\text{SMC}}_{\text{MMP}-2}(\tau) + m^{\text{SMC}}_{\text{MMP}-2}(\sigma_\theta)$ in $[\text{fg}\cdot\text{h}^{-1}]$. $m^{\text{SMC}}_{\text{MMP}-2}(\tau)$ is the WSS-driven mass of MMP-2 released by the SMCs (Reda et al. 2022) and $m^{\text{SMC}}_{\text{MMP}-2}(\sigma_\theta)$ is defined by equation (4).

And lastly, the probability of elastin degradation by one SMC modulated by MMP-2 and MMP-9 is described as follows:

$$\mathcal{D}^{\text{e}}(\tau,\sigma_\theta) = \mathcal{D}^{\text{e}}_{\text{MMP}-2}(\tau,\sigma_\theta) + \mathcal{D}^{\text{e}}_{\text{MMP}-9}(\sigma_\theta) \tag{7}$$

$$\mathcal{D}^{\text{e}}_{\text{MMP}-2}(\tau,\sigma_\theta) = \gamma_{\text{MMP}-2} \times m_{\text{MMP}-2}(\tau,\sigma_\theta) \tag{8}$$

$$\mathcal{D}^{\text{e}}_{\text{MMP}-9}(\sigma_\theta) = \gamma_{\text{MMP}-9} \times m^{\text{SMC}}_{\text{MMP}-9}(\sigma_\theta) \tag{9}$$

where $m_{\text{MMP}-2}(\tau,\sigma_\theta) = m^{\text{SMC}}_{\text{MMP}-2}(\tau) + m^{\text{SMC}}_{\text{MMP}-2}(\sigma_\theta)$ in $[\text{fg}\cdot\text{h}^{-1}]$ as previously defined in equation (6) and $m^{\text{SMC}}_{\text{MMP}-9}(\sigma_\theta)$ in $[\text{fg}\cdot\text{h}^{-1}]$ is expressed by equation (3), $\gamma_{\text{MMP}-2} = 3,14\times10^{-6}$ fg^{-1}, $\gamma_{\text{MMP}-9} = 1,036\times10^{-6}$ fg^{-1}.

Similarly to the SMCs' probability of proliferation, the organization of the extracellular matrix is governed by mechanical constraints, and is thus intrinsically linked to the choice of the mechanical constitutive law.

2.2 Finite Element Model

As shown in the previous section, the circumferential stress field generated by blood pressure within the arterial wall plays a central role in modulating cellular mechanisms involved in intimal hyperplasia. Actually, the proliferation of SMCs as well as matrix metalloproteinase (MMP) secretion by SMCs, responsible for collagen and elastin degradation, is stimulated when circumferential stresses exceed their homeostatic values. Likewise, reduced circumferential stress can further promote MMP secretion, leading to medial atrophy. For this reason, a finite element model was developed to compute the stress distribution across the arterial wall and provide inputs to the ABM.

Finite Element implementation: The circumferential stress field σ_θ was computed with FEniCS in the arterial media layer. FEniCs is an open-source framework for solving partial differential equations with the finite element method (Alnæs et al. 2015). An intraluminal pressure of 13.3 kPa was applied, generating an initial stress

field that progressively evolves with wall thickening during long-term intimal hyperplasia. Based on the principle of virtual work, the mixed variational formulation for static incompressible hyperelasticity (introducing a Lagrange multiplier p) seeks the displacement–pressure pair $(\mathbf{u}, p) \in \mathbf{V} \times Q$, with $\mathbf{V}$ and Q the respective functional spaces for displacement and pressure, such that for all virtual displacement field $\delta\mathbf{u} \in \mathbf{V}$ and virtual pressure field $\delta p \in Q$, the following equations have to be satisfied on the entire artery domain Ω (Wriggers 2008):

$$\int_\Omega \frac{\partial \Psi(\mathbf{F})}{\partial \mathbf{F}} : \nabla \delta\mathbf{u} \, d\Omega - \int_\Omega p \, \mathbf{F}^{-T} : \nabla \delta\mathbf{u} \, d\Omega = \int_\Omega \mathbf{b} \cdot \delta\mathbf{u} \, d\Omega + \int_\Gamma \mathbf{t} \cdot \delta\mathbf{u} \, d\Gamma \tag{10}$$

$$\int_\Omega \delta p \, (\det(\mathbf{F}) - 1) \, d\Omega = 0 \tag{11}$$

where $\Psi(\mathbf{F})$ denotes the strain energy density as a function of the deformation gradient $\mathbf{F} = \nabla\mathbf{u}$, p is the Lagrange multiplier (pressure), $\mathbf{b}$ the body force vector, and $\mathbf{t}$ the traction vector prescribed on the boundary Γ of Ω. The operator " $\cdot$ " stands for the scalar product between two vectors, " : " designates the double contraction product of two tensors, and ∇ is the spatial gradient operator.

Constitutive laws: To assess the effect of arterial mechanical behavior on stress-mediated remodeling, three constitutive laws were tested: linear elastic, hyperelastic isotropic and hyperelastic anisotropic behaviours.
For the linear elastic isotrope constitutive law, a Young's modulus equal to 454.7 kPa was taken as for coronary arteries (Noble et al. 2020).
For the hyperelastic isotropic behaviour, the Neo-Hookean law was implemented as follows:

$$\Psi(I_1) = c_{10}(I_1 - 3) \tag{12}$$

with $I_1 = \mathrm{tr}\,(\mathbf{C})$ is the first invariant of the right Cauchy-Green deformation tensor $\mathbf{C}$, $\mathrm{tr}\,(\mathbf{C})$ is the trace of $\mathbf{C}$, and $c_{10} = 21.62$ kPa (Noble et al. 2020).
Arteries exhibit a strongly anisotropic hyperelastic response, primarily due to the arrangement of collagen fibers. To capture this effect, we implemented in FEniCS the Holzapfel-Gasser-Ogden (HGO) model, which explicitly accounts for helically oriented fiber families within the arterial wall. In the present work, the formulation was restricted to the media layer, but it naturally generalizes to multiple families, such as those in the adventitia. For a single fiber family in the media, the strain energy density takes the form (Gasser et al. 2006):

$$\Psi(I_1, I_4) = c_{01}(I_1 - 3) + \frac{k_1}{2k_2}\left[\exp\left\{k_2\left[\kappa I_1 + (1 - 3\kappa)I_4 - 1\right]^2\right\} - 1\right] \tag{13}$$

$I_4 = \mathbf{a_0} \cdot \mathbf{C} \cdot \mathbf{a_0} = \lambda_f^2$ is the anisotropic invariant representing the squared stretch of the fibers (λ_f^2) in the direction $\mathbf{a_0} = [0, \cos(\beta), \sin(\beta)]^T$, β is the direction of the fibers (Gasser et al. 2006). The remaining constants are material parameters of the constitutive law given in Table 1 (Schiavone and Zhao 2015).

Table 1 Material parameters used for the anisotropic law (Gasser et al. 2006) implemented in FEniCS.

	c_{10} [kPa]	k_1 [kPa]	k_2 [-]	κ [-]	β	Reference
Anisotropic model	1,4	180	100	0,314	49,98°	(Schiavone and Zhao 2015)

Material parameters were taken from experimental data on coronary arteries, which share similar mechanical properties with digital arteries. The stress distributions obtained with these constitutive laws differed markedly, with isotropic models predicting narrower stress ranges compared to the highly nonuniform distribution produced by the anisotropic model. Consequently, the values of $\sigma_{\min}$ and $\sigma_{\max}$ used in the ABM rules for stress-regulated secretion were updated according to the constitutive law selected in the FE model.

2.3 ABM-FEM framework

The coupling between the ABM and the FEM involved iterative data exchange. The ABM generated the arterial geometry in NetLogo, which was then imported into FEniCS to construct the FEM and simulate circumferential stresses. These stress values were subsequently reintroduced into the ABM as cell-specific variables, updating the mechanoregulation of biological processes (Figure 2). A new stress field was computed at each coupling step based on the updated geometry resulting from ABM-driven growth.

Communication between NetLogo and FEniCS was implemented in Python using the PyNetLogo package (Jaxa-Rozen and Kwakkel 2018), which allows controlling NetLogo from Python. The coupling was automated and occurred at defined intervals, controlled by a coupling index k and a time duration T per iteration. The simulation framework looped over iterations in Python, keeping the WSS constant during each T to represent physiological or vibration-induced conditions.

At each iteration, the ABM governed cellular behaviors including SMC proliferation, migration, and ECM secretion/degradation through probabilistic rules, derived from experimental observations and literature. Circumferential stresses computed by the FEM were fed back into the ABM, regulating biological phenomena such as the secretion of growth factors and MMPs by SMCs. In uncoupled simulations, stress values remained identical to those of the previous iteration. WSS varied dynamically with each iteration to capture cycles of vibration exposure and their effects on arterial remodeling.

Discrete cell movements inside the artery can create geometric spikes (breaking the continuous endothelium) at the boundaries, particularly at the lumen interface, which can compromise the axisymmetric geometry of the model and produce non-biological shapes (Corti et al. 2020). These irregularities can distort local mechanical interactions and affect the accuracy of predicted cellular behaviors if not corrected. To maintain a compact and biologically realistic structure, the model applied a smoothing algorithm to the arterial interfaces after each iteration. This regularization process rearranged

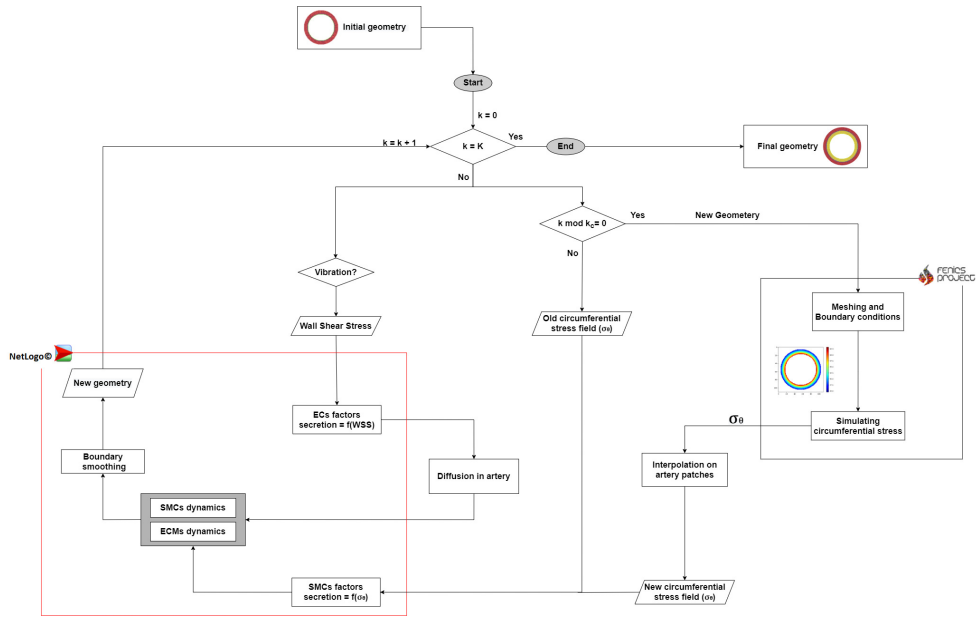

Fig. 2 ABM-FEM framework. At each iteration, cellular mechanisms are computed in the ABM. At each coupling step, the circumferential stress is updated in the FEM and introduced again in the ABM.

cells to increase their contact surface, while preserving the movement of internal elastic lamellae (IEL), which can be displaced by medial growth without being crossed by migrating SMCs (Reda et al. 2020).

The model was initialized in a physiological state ($\tau = 3$ Pa), and vibration-induced intimal hyperplasia was triggered by lowering WSS to 1 Pa, simulating prolonged hand-arm vibration exposure (4h/day). Due to the stochastic nature of certain biological processes, multiple simulations were performed for each condition, and results were averaged for robustness. All governing equations, model parameters, and agent behavior rules are provided in Appendix A of (Reda et al. 2022).

3 Results

3.1 Basal versus vibration exposure states for linear elastic artery

Bootstrap analysis of our ABM showed that relative errors in SMC and collagen counts stabilized after approximately 10 simulations, with average errors of 0.8% for SMCs and 2.5% for collagen over 10 years (Reda et al. 2022). Consequently, all results are reported as the mean of 10 simulations with 95% confidence intervals, normalized to initial values.

In this section, the artery was supposed to behave like a linear elastic material with a Young's modulus taken equal to 454.7 kPa as for coronary artery (Noble et al.

2020). A coupling time of one week was selected, as it provided similar results to shorter intervals while greatly reducing computational cost.

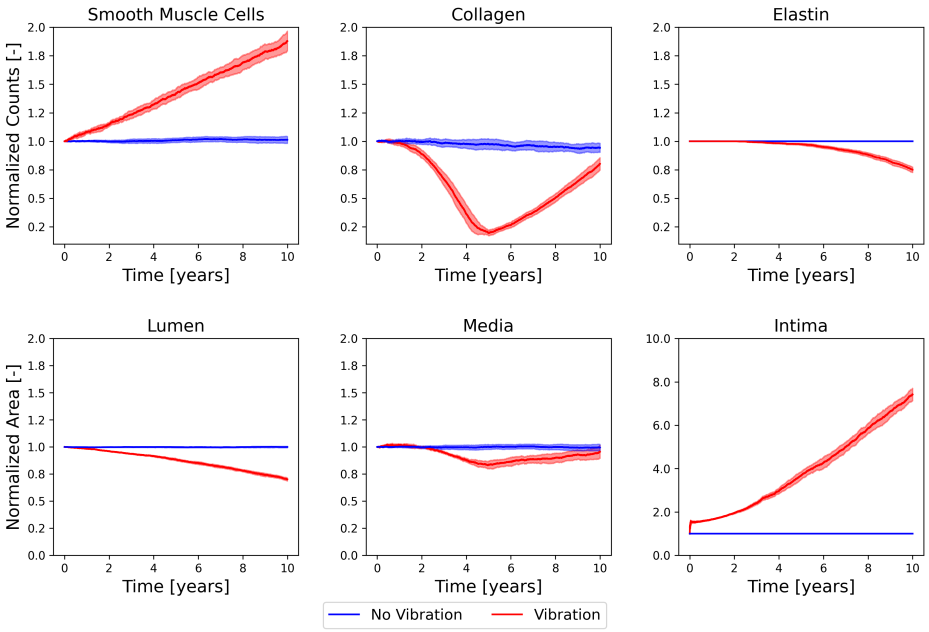

Fig. 3 Normalized counts of SMCs (top left), collagen (top middle), and elastin (top right) agents, together with normalized lumen (bottom left), media (bottom middle), and intima (bottom right) areas, as a function of time in the vibration and basal states. The shaded areas match the 95% confidence interval.

Figure 3 shows the effects of vibration-induced WSS and circumferential stresses on cellular mechanisms and layers thicknesses. Under baseline conditions (No Vibration), the artery preserved its geometry, layer thicknesses, and constant counts of SMCs, collagen and elastin. In contrast, chronic exposure to vibration over 10 years led to the formation of symmetrical intimal hyperplasia, characterized by a 30% reduction in lumen area and an increase in intimal thickness. Mechanoregulated cellular responses produced an initial decrease followed by an increase in total collagen, accompanied by a reduction in the media area. SMC counts approximately doubled, while elastin degradation became noticeable after 5 years. These results highlighted the model's ability to reproduce both physiological stability and vibration-induced vascular remodeling. SMC count increased due to the increase in growth factors secretion leading to SMC proliferation. The initial decrease in collagen counts was due to the decrease of the circumferential stress values in the arterial layers as the intimal hyperplasia started forming and thus increasing the thickness of the arterial wall.

3.2 Influence of the degradation rate of MMP-2 for linear elastic artery

In our ABM, circumferential stress acts as a key regulator of ECM remodeling. From equation (4), the secretion of MMP-2, which is an agent that degrades collagen and elastin, increased when the circumferential stress and WSS decreased. To capture the natural elimination of MMP-2, the model incorporates a degradation rate of 1% per hour, consistent with the arterial growth model proposed by (Zahedmanesh and Lally 2012). However, other studies have implemented much faster degradation rates, up to 50% per hour (Keshavarzian et al. 2018). To investigate the sensitivity of our model to this parameter, we compared simulations with both values. A decrease in circumferential stress stimulates SMCs to secrete MMP-2. Consequently, as circumferential stress diminishes during arterial growth, the cumulative secretion of MMP-2 by SMCs increases (Figure 4). This results in progressive degradation of both collagen and

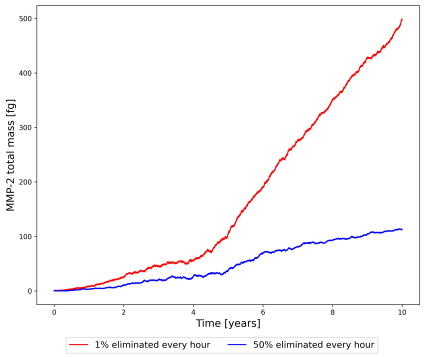

Fig. 4 MMP-2 mass secreted over 10 years of simulation for two different degradation rates.

elastin, with collagen being more rapidly affected due to its higher susceptibility to MMP-2 (Figure 5, left and middle). In both MMP-2 degradation rates, collagen elimination in the media was significant. Nevertheless, when the degradation rate was slower (1% per hour), MMP-2 accumulated in greater amounts over time (Figure 4), leading not only to faster and more complete collagen degradation (Figure 5, left) but also to a stronger effect on elastin breakdown (Figure 5, middle) and a more pronounced thinning of the media layer (Figure 5, right). By contrast, the faster degradation rate (50% per hour) limited enzyme accumulation; however, even at these reduced levels, MMP-2 was sufficient to induce observable collagen degradation (Figure 5, left), though with a lesser impact on elastin (Figure 5, middle).

Overall, these findings demonstrate that the dynamics of MMP-2 clearance strongly influence the balance between collagen and elastin degradation. A slower degradation rate promotes enzyme accumulation and thereby accelerates ECM remodeling, while a faster degradation rate reduces accumulation but does not prevent significant collagen loss. This highlights the critical role of MMP-2 kinetics in the long-term remodeling of the arterial wall under reduced circumferential stress.

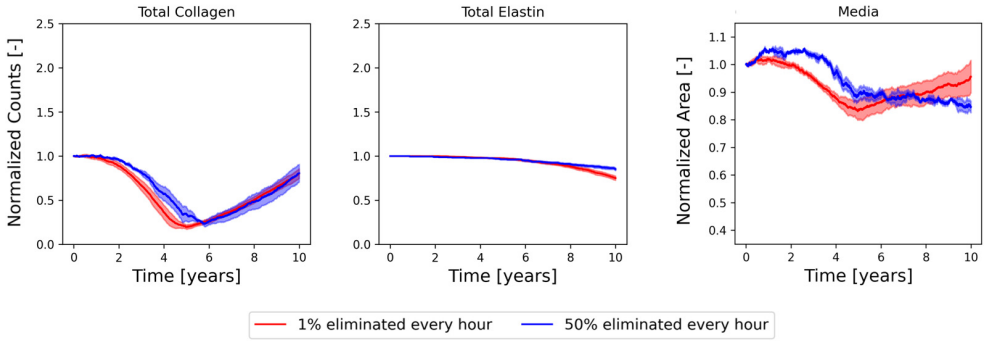

Fig. 5 Normalized counts of collagen and elastin agents, and normalized media area, as a function of time for two different degradation rates of MMP-2. The shaded areas represent the 95% confidence interval.

3.3 Influence of the Mechanical Constitutive Law of the Artery

The influence of the mechanical behavior of the artery on the evolution of the system over 5 years was studied. We tested two mechanical hyperelastic constitutive laws, isotropic Neo-Hookean and anisotropic HGO, often used for the modeling of the mechanical behavior of the artery (Keshavarzian et al. 2018, 2019) and detailed earlier. First, the distribution of the stress field across the arterial wall thickness at $k = 0$ varies depending on the constitutive law employed (Figure 6). Moreover, we observe

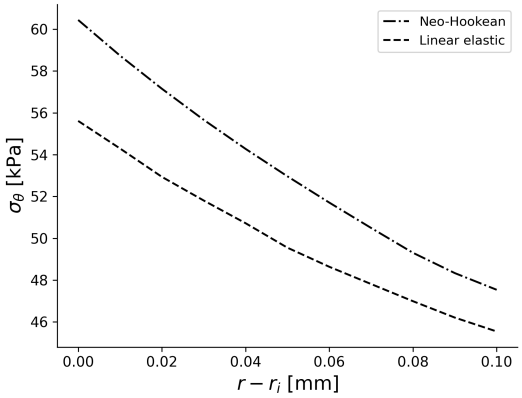

Fig. 6 Distribution of circumferential stresses across the arterial wall thickness for a linear elastic law and a Neo-Hookean law at the first computation step $k = 0$. r is the artery radius and r_i is the internal artery radius.

that the minimum ($\sigma_{\min}$) and maximum ($\sigma_{\max}$) values of the circumferential stresses within the arterial wall also vary according to the mechanical constitutive law and the associated parameters. For a linear elastic law, we obtain $\sigma_{\min} = 45.5$ kPa and

$\sigma_{\max} = 55.5$ kPa, whereas for a Neo-Hookean law the values are $\sigma_{\min} = 47.5$ kPa and $\sigma_{\max} = 62.5$ kPa.

In contrast, Figure 7 shows the distribution of circumferential stresses across the arterial wall thickness for the anisotropic law. Unlike isotropic laws, the stress distribution across the thickness of an anisotropic artery is not uniform with respect to the angle θ. The minimum and maximum stress values in the case of anisotropic mechanical behavior are given by: $\sigma_{\min} = 38$ kPa and $\sigma_{\max} = 190$ kPa.

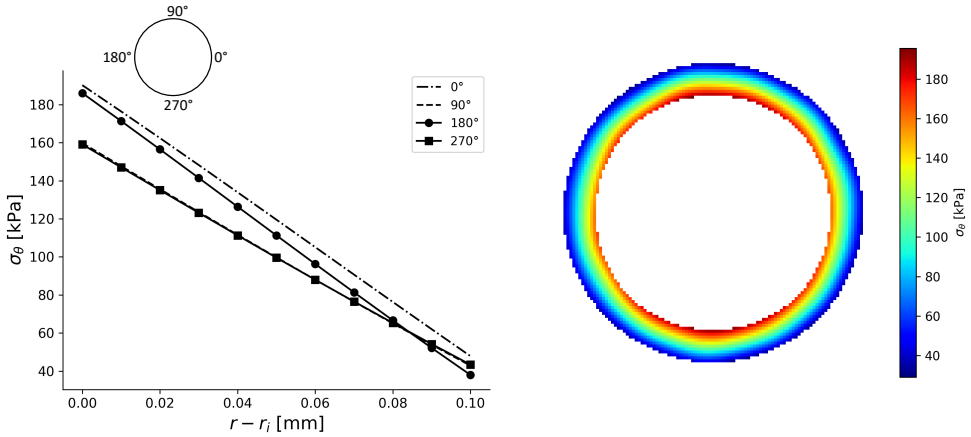

Fig. 7 Distribution of the circumferential stress field across the arterial wall thickness for the anisotropic hyperelastic law at $k = 0$. Left: σ_θ in the media thickness at different angular positions. r is the artery radius and r_i is the internal artery radius. Right: mapping of the circumferential stress field.

Depending on the chosen constitutive law, the values of $\sigma_{\min}$ and $\sigma_{\max}$ were updated in the ABM rules and the circumferential stress field was computed according to the selected law.

The variations in the number of agents over time are comparable for the three laws considered (top views shown in Figure 8). Furthermore, the predicted rate of arterial stenosis (Figure 8 bottom left) is nearly identical for all three laws.

Table 2 summarizes model outputs predicted by the WSS-only ABM developed previously (Reda et al. 2022) and by the present mechanobiological framework including circumferential stress mechanoregulation. The comparison highlights the influence of the FEM coupling on ECM remodeling and media atrophy.

3.4 Influence of the Minimum Limit Value of Circumferential Stresses

In our model, the rules for mechanoregulated biological phenomena are implemented based on the two minimum ($\sigma_{\min}$) and maximum ($\sigma_{\max}$) limit values of the circumferential stress field. These values are derived from the stress field obtained within the healthy arterial wall (computed at $k = 0$) and depend on the applied mechanical constitutive law. For example, for a linear elastic law, we used $\sigma_{\min} = 45.5$ kPa

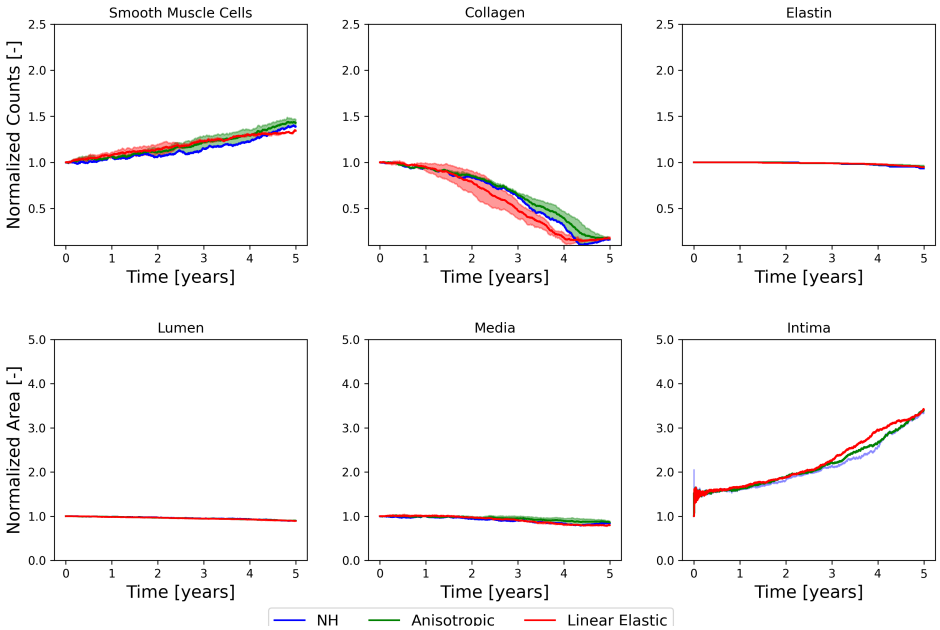

Fig. 8 Variations in the number of agents and arterial layer thicknesses over time for the linear elastic law, the Neo-Hookean hyperelastic law and the anisotropic law. The shaded areas match the 95% confidence interval.

Table 2 Comparison of the main normalized model outputs predicted by the WSS-driven ABM (Reda et al. 2022) and the present ABM-FEM framework after 5 years of simulation.

Model output	WSS-only ABM	ABM-FEM
Predicted stenosis rate	14% ± 0.034	11% ± 0.003
Normalized SMC counts	1.44 ± 0.14	1.42 ± 0.08
Normalized Collagen counts	1.22 ± 0.1	0.16 ± 0.066
Normalized Media area	1.08 ± 0.13	0.86 ± 0.08

and $\sigma_{\max} = 55.5$ kPa. Since our model application involves a decrease in circumferential stresses during growth, we chose to study the influence of $\sigma_{\min}$ on the system's evolution. The model was then simulated considering an alternative value for the minimum stress limit of $\sigma_{\min} = 35$ kPa. This value is used by (Boyle et al. 2010) in their restenosis model.

The choice of $\sigma_{\min}$ has a significant effect on collagen degradation over time (Figure 9 top middle). For a $\sigma_{\min}$ value of 35 kPa, which is lower than the minimum value calculated at $k = 0$, the decrease in stresses during growth does not immediately reach the threshold for triggering mechanoregulated biological phenomena, and the system

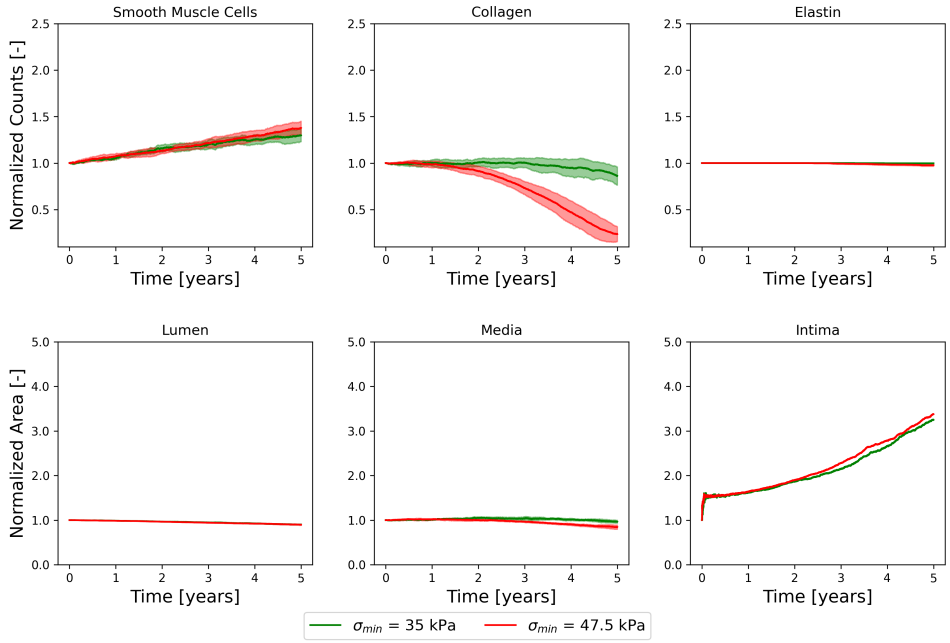

Fig. 9 Influence of the value of $\sigma_{\min}$ on the evolution of the system over time in the case of a linear elastic artery. The shaded areas match the 95% confidence interval.

remains at basal stress values for a longer period, during which collagen degradation does not occur. No significant difference occurs for the other quantities.

3.5 Influence of the surrounding tissues

In true condition, the digital artery is surrounded by soft tissues. This may alter the stress field generated within the artery. Therefore, the presence of soft tissues around the artery was considered in order to study their influence on the development of intimal hyperplasia.

The FEM of the artery was then integrated into a tissue model that simulates the presence of soft tissues. The presence of the bone at a distance $L = 2 \times D$ from the center of the artery, where D is the diameter of the artery, was modeled by applying a zero-displacement condition on one of the boundaries of the model (Γ_{bone} on Figure 10 top view). The artery and the flesh were assumed to behave like an elastic isotropic material with Young moduli of respectively 454.7 kPa (Noble et al. 2020) and 13 kPa (Noël 2018).

The stress values differ between the two boundary condition cases, being lower when the surrounding flesh is taken into account (Figure 10, bottom left). Additionally, the stress distribution is not uniform with respect to the rotational angle θ, indicating anisotropy caused by the presence of the surrounding tissue.

We then simulated intimal hyperplasia for both the artery alone and the artery surrounded by flesh. The minimum and maximum stress values were also adjusted

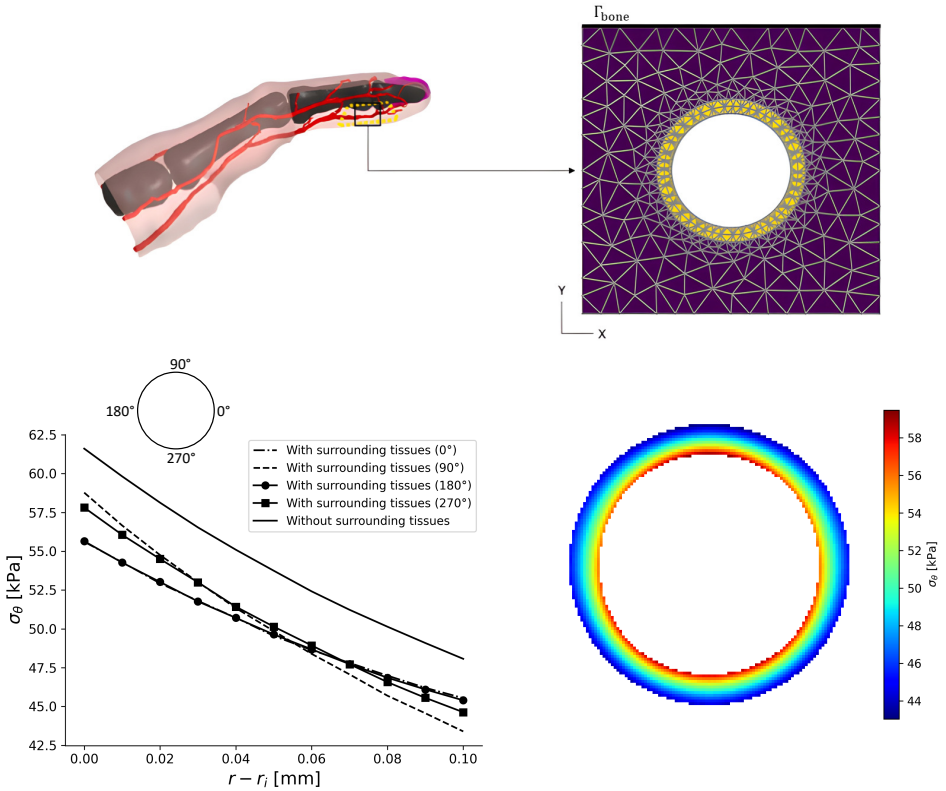

Fig. 10 Top view: Finite element mesh and boundary conditions, showing the soft tissue and the boundary where zero displacement is imposed to represent the underlying bone in the finger. Bottom view: Distribution of the circumferential stress field across the arterial wall thickness surrounded by soft tissue at $k = 0$. Left: σ_θ in the media thickness at different angular positions. r is the artery radius, and r_i the internal artery radius. Right: mapping of the circumferential stress field.

based on the specific case being tested. The simulations indicate that the system's behavior is similar in both scenarios, for SMCs counts, collagen and elastin amount, as well as lumen, media, and intima growth, suggesting that the presence of soft tissues does not influence the system's evolution over the 5-year simulation period (Figure 11).

4 Discussion

Our finite element mechanical model offers the advantage of incorporating constitutive laws tailored to the hyperelastic and anisotropic nature of arterial tissue, rather than relying on oversimplified linear elastic assumptions. Integrating this model with the ABM allows for the estimation of circumferential stress fields that more realistically capture arterial behavior as governed by the selected material formulation. Although quantitative clinical measurements of stenosis progression in HAV-exposed digital

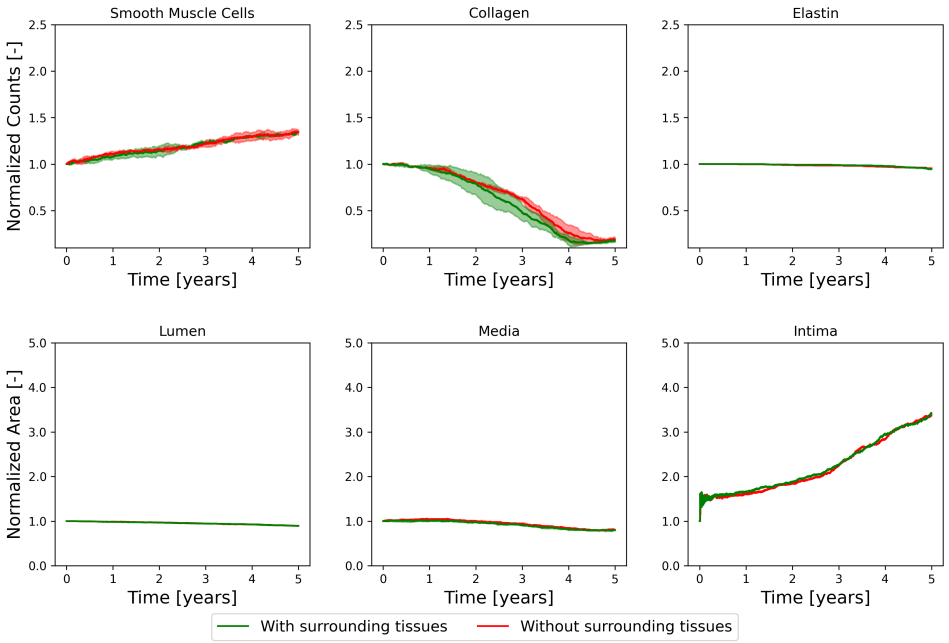

Fig. 11 Variation of agent counts and normalized arterial layer areas over time for the cases of an isolated artery and an artery surrounded by soft tissue. The shaded areas match the 95% confidence interval.

arteries remain scarce, the predicted lumen narrowing and media remodeling are consistent with experimental and histological observations reported in vibration-induced vascular disease (Okada et al. 1987; Takeuchi et al. 1985).

However, our simulations highlighted that the selected material law for modeling arterial mechanical behavior does not influence development of arterial stenosis during the five-year calculation period. Moreover, in this study, for all the tested laws, the pressure applied to the endothelium to simulate the stress field was kept constant at its homeostatic baseline value of P = 13.3 kPa. This is a strong assumption that implies that blood pressure remains constant over time and does not change even as the artery's geometry varies. In the short term, blood pressure fluctuates during the cardiac cycle, between systole (P = 16 kPa) and diastole (P = 10.6 kPa), and these variations could potentially affect the stress field values during the cycle. Furthermore, blood pressure changes with age and geometric modifications, which was not considered in our model. Thus, applying constant blood pressure during growth led to a decrease in circumferential stress as arterial thickness increased. The mechanobiological model results showed that this reduction had the most significant effect on collagen degradation in the artery, a result also highlighted by (Bayer et al. 1999) in their study on the atrophic effect of reduced circumferential stress on the media. These results might change if a time-varying pressure value were taken into account. Also, our simulations predicted elastin degradation, in agreement with the observations reported by (Takeuchi et al. 1985) in patients with vibration-induced Raynaud's syndrome. In

addition, vibration exposure was not modeled as a direct mechanical loading applied to the arterial wall, but rather indirectly through a step reduction in WSS. Consequently, the FEM was formulated under quasi-static conditions in order to focus on long-term arterial remodeling processes. Hence, averaged mechanical quantities were considered sufficient within the scope of the present framework.

We also demonstrated that considering the surrounding environment of the artery, composed of soft tissue, had no significant impact on the development of intimal hyperplasia. However, the presence of soft tissue, along with the boundary condition simulating the presence of bone, induced anisotropy to the stress field distribution within the artery. Consequently, these results indicate that the surrounding environment should be accounted for in future studies on non-uniform arterial growth.

Finally, we hypothesize that the model's insensitivity to mechanical material laws and boundary conditions arises from the rules implemented in the ABM, which depend on the minimum and maximum circumferential stress values for triggering phenomena related to atrophy. Due to a lack of experimental data on these limits, we assumed that they correspond to the minimum and maximum stress values generated in the artery for each material law. Therefore, these limits were adjusted based on the stress field obtained for each law. To study the influence of the minimum threshold value σ_{min} on system evolution, we simulated the intimal hyperplasia model using a value from the growth model of (Boyle et al. 2010), set at $\sigma_{min} = 35$ kPa. The numerical results show reduced collagen degradation over time when a lower σ_{min} threshold is used. This study highlights the importance of this threshold on arterial remodeling in response to decreased circumferential stress. Estimating this value requires experimental studies to determine the minimum stress value to which SMCs can be exposed before they switch to a secretory phenotype. These results also suggest that, within the present framework, biochemical regulation plays a more dominant role in remodeling progression than the specific constitutive behavior of the arterial wall. Although the different material laws generated distinct circumferential stress distributions, the associated biological response remained relatively similar because the mechanoregulation rules were driven primarily by deviations from physiological stress thresholds rather than by the exact local stress magnitudes. A more robust experimental identification and calibration of the mechanoregulation thresholds would constitute an important next step for the present framework. Such calibration would also allow a more systematic investigation of the influence of material parameters and constitutive laws on arterial remodeling through dedicated sensitivity analyses.

Moreover, it should be noted that the material laws do not account for residual stresses within the artery or the active behavior of SMCs, which may also affect the minimum or maximum values considered in modeling intimal hyperplasia.

One of the advantages of our model is its potential to integrate other biological mechanisms at different scales which take into account patient-specific characteristics, such as age, smoking habits, or cholesterol levels-factors likely to influence arterial growth (Wang et al. 2021; Hao and Friedman 2014).

5 Limitations

Although our model is capable of simulating the development of intimal hyperplasia induced by vibrations transmitted to the hand-arm system, it was built on strong assumptions and ignored certain aspects that could have affected the model's final outcome.

First, the WSS values used to describe the presence or absence of vibrations (with $\tau = 1$ Pa and $\tau = 3$ Pa) were imposed as two constant and uniform values on the endothelium. This assumed that the arterial growth simulated by our model is uniform. In fact, arterial histologies after growth show anisotropy in intimal thickening, where the growth rate is greater in some areas than others (Corti et al. 2020). A section of a real artery's geometry exhibits geometric nonuniformities that can affect blood flow and potentially alter the contour of WSS values on the endothelium. To overcome these limitations, future developments of the framework will include coupling with a computational fluid dynamics model capable of providing geometry-dependent WSS distributions. Such coupling would allow the WSS profile to evolve continuously with arterial geometry during remodeling. Furthermore, this approach could help identify arterial regions most susceptible to the onset of intimal hyperplasia.

Additionally, the assumption of a 2D geometry presents a major limitation of the model. Indeed, developing the model with a 3D geometry would provide more information on the system's evolution. For example, mediator diffusion through the arterial layers in a 3D geometry more closely aligns with biological reality and allows for the study of cell behavior along the longitudinal direction. Furthermore, a geometrical smoothing procedure was applied during simulations in order to limit numerically induced anisotropies resulting from the lattice discretization. While this regularization step improves numerical stability and maintains a physiologically realistic arterial shape during growth, it may also reduce the development of local geometric irregularities and stress concentrations that could occur in real arteries.

Moreover, in our current model, the adventitia layer was ignored. In a real artery, biochemical exchanges may occur between the adventitia and media. Furthermore, adding the adventitia layer could influence the circumferential stress field in the arterial wall. Therefore, considering the adventitia layer and identifying the biological processes involved in intimal hyperplasia at this level could form the basis of future work to enhance the model's predictive capabilities. Furthermore, due to the lack of experimentally identified constitutive parameters for human digital arteries, the material parameters used in the present study were derived from coronary artery data. This choice was motivated by the fact that both coronary and digital arteries are muscular arteries and share similar structural and mechanical characteristics (Noble et al. 2020). Nevertheless, experimental characterization of the mechanical behavior of digital arteries would improve the physiological specificity of the model and refine the predicted stress distributions. Future developments will also include sensitivity and uncertainty analyses in order to identify the most influential mechanobiological drivers governing arterial remodeling and stenosis progression.

In addition, our model assumes that the arterial stenosis observed in patients with vibratory Raynaud's syndrome is caused by intimal hyperplasia only. However, biopsies from patients with this syndrome sometimes reveal the infiltration and accumulation

of leukocytes in the intima (Gayraud 2007; Stoyneva et al. 2003). These processes were not incorporated into our model, although they may have affected the ultimate arterial stenosis outcome.

Besides, our study ignored biological mechanisms related to the natural aging of the artery, such as the increase in basal collagen degradation over time (Panwar et al. 2018). We kept our parameters constant throughout the simulation period, as we assumed that changes due to aging between five and ten years were negligible. However, for longer simulation durations, accounting for these aging mechanisms would lead to more precise and realistic predictions.

Finally, the coupling time between both models was optimized and the code was parallelized when possible in order to reduce the computational load ($\geq$ 12h for one simulation). However, our speed analysis showed that this load relies mainly in the communication routines between NetLogo and Python (Reda et al. 2022). Therefore, future improvements should aim at reducing this cost by limiting both models to one computational environment only.

6 Conclusion

The developed mechanobiological model was able to maintain a steady state in the non-vibratory condition and predict the development of intimal hyperplasia under vibratory conditions, describing a daily cycle of exposure to vibrations. Incorporating circumferential stresses (σ_θ), often overlooked in existing models of hemodynamically induced intimal hyperplasia, highlighted the mechano-regulation (influence of σ_θ) of the biological phenomena involved in intimal hyperplasia. Our model predicted an arterial stenosis rate of 30% after ten years of simulation with four hours of daily vibration exposure. The degradation of the extracellular matrix (ECM) in the media was evidenced by the decreasing values of σ_θ during arterial growth. This study also demonstrated the effect of the natural degradation rate of the MMP-2 enzyme, responsible for ECM degradation, on the accumulation of its total mass over time.

Furthermore, we studied the model's sensitivity to the mechanical constitutive law of the artery. To do this, coupling between the mechanobiological finite element (FE) models was performed weekly during the five-year simulation period. Our study showed that while the distribution of circumferential stress fields changes depending on the constitutive law considered, this change does not affect the prediction of the mechanobiological model over the five-year simulation period. This is due to the calibration of the parameters ($\sigma_{\min}$ and $\sigma_{\max}$) of the mechanoregulated biological phenomena based on the stress field obtained for each behavior law. In the case of decreasing circumferential stresses during growth, a more accurate knowledge of the minimum limit value ($\sigma_{\min}$) could yield different results, as demonstrated in our findings, thereby increasing confidence in the model's predictions.

Finally, the creation of a database for predicting arterial stenosis rates (i.e., the Vibration White Finger stages) based on daily exposure duration and WSS values is currently being developed. The ultimate goal would be to redefine a daily vibration dose aimed at better protecting workers against vascular pathologies caused by using hand-held or hand-guided vibrating machines.

Declarations

- Funding No funding was received to assist with the preparation of this manuscript.
- Conflict of interest/Competing interests The authors have no competing interests to declare that are relevant to the content of this article.
- Ethics approval and consent to participate Not applicable
- Consent for publication Not applicable
- Data availability Not applicable
- Code availability Codes used in the current study are available from the corresponding author on reasonable request.
- Author contribution All authors contributed to the study conception and design. Methodology, formal analysis and investigation were performed by M.R. and C.N. The first draft of the manuscript was written by M.R. and all authors commented on previous versions of the manuscript. All authors read and approved the final manuscript.

References

Alnæs, M., Blechta, J., Hake, J., Johansson, A., Kehlet, B., Logg, A., Richardson, C., Ring, J., Rognes, M.E., Wells, G.N.: The FEniCS project version 1.5. Archive of numerical software **3**(100) (2015) https://doi.org/10.11588/ans.2015.100.20553

Andrews, A.M., Jaron, D., Buerk, D.G., Kirby, P.L., Barbee, K.A.: Direct, real-time measurement of shear stress-induced nitric oxide produced from endothelial cells in vitro. Nitric Oxide - Biology and Chemistry **23**(4), 335–342 (2010) https://doi.org/10.1016/j.niox.2010.08.003

Bayer, I.M., Adamson, S.L., Langille, B.L.: Atrophic remodeling of the artery-cuffed artery. Arteriosclerosis, Thrombosis, and Vascular Biology **19**(6), 1499–1505 (1999) https://doi.org/10.1161/01.ATV.19.6.1499

Boyle, C.J., Lennon, A.B., Early, M., Kelly, D.J., Lally, C., Prendergast, P.J.: Computational simulation methodologies for mechanobiological modelling: A cell-centred approach to neointima development in stents. Philosophical Transactions of the Royal Society A: Mathematical, Physical and Engineering Sciences **368**(1921), 2919–2935 (2010) https://doi.org/10.1098/rsta.2010.0071

Bornfeldt, K.E., Raines, E.W., Nakano, T., Graves, L.M., Krebs, E.G., Ross, R.: Insulin-like growth factor-I and platelet-derived growth factor-BB induce directed migration of human arterial smooth muscle cells via signaling pathways that are distinct from those of proliferation. Journal of Clinical Investigation **93**(3), 1266–1274 (1994) https://doi.org/10.1172/JCI117081

Brammer, A.J., Taylor, W., Lundborg, G.: Sensorineural stages of the hand-arm vibration syndrome. Scandinavian Journal of Work, Environment and Health **13**(4), 279–283 (1987) https://doi.org/10.5271/sjweh.2050

Curry, B.D., Bain, J.L.W., Yan, J.G., Zhang, L.L., Yamaguchi, M., Matloub, H.S., Riley, D.A.: Vibration injury damages arterial endothelial cells. Muscle and Nerve **25**(4), 527–534 (2002) https://doi.org/10.1002/mus.10058

Corti, A., Chiastra, C., Colombo, M., Garbey, M., Migliavacca, F., Casarin, S.: A fully coupled computational fluid dynamics – agent-based model of atherosclerotic plaque development: Multiscale modeling framework and parameter sensitivity analysis. Computers in Biology and Medicine **118**(November 2019), 103623 (2020) https://doi.org/10.1016/j.compbiomed.2020.103623

Corti, A., Colombo, M., Migliavacca, F., Rodriguez Matas, J.F., Casarin, S., Chiastra, C.: Multiscale Computational Modeling of Vascular Adaptation: A Systems Biology Approach Using Agent-Based Models. Frontiers in Bioengineering and Biotechnology **9**(November), 1–27 (2021) https://doi.org/10.3389/fbioe.2021.744560

Caiazzo, A., Evans, D., Falcone, J.L., Hegewald, J., Lorenz, E., Stahl, B., Wang, D., Bernsdorf, J., Chopard, B., Gunn, J., Hose, R., Krafczyk, M., Lawford, P., Smallwood, R., Walker, D., Hoekstra, A.: A Complex Automata approach for in-stent restenosis: Two-dimensional multiscale modelling and simulations. Journal of Computational Science **2**(1), 9–17 (2011) https://doi.org/10.1016/j.jocs.2010.09.002

Cucina, A., Sterpetti, A.V., Borrelli, V., Pagliei, S., Cavallaro, A., D'Angelo, L.S.: Shear stress induces transforming growth factor-beta1 release by arterial endothelial cells. Surgery **123**(2), 212–217 (1998) https://doi.org/10.1016/S0039-6060(98)70260-0

Dardik, A., Yamashita, A., Aziz, F., Asada, H., Sumpio, B.E.: Shear stress-stimulated endothelial cells induce smooth muscle cell chemotaxis via platelet-derived growth factor-BB and interleukin-1α. Journal of Vascular Surgery **41**(2), 321–331 (2005) https://doi.org/10.1016/j.jvs.2004.11.016

Epstein, F.H., Gibbons, G.H., Dzau, V.J.: The emerging concept of vascular remodeling. New England Journal of Medicine **330**(20), 1431–1438 (1994) https://doi.org/10.1056/NEJM199405193302008

Gayraud, M.: Raynaud's phenomenon. Joint Bone Spine **74**, 1–7 (2007) https://doi.org/10.1016/j.jbspin.2006.07.002

Gasser, T.C., Ogden, R.W., Holzapfel, G.A.: Hyperelastic modelling of arterial layers with distributed collagen fibre orientations. Journal of the Royal Society Interface **3**(6), 15–35 (2006) https://doi.org/10.1098/rsif.2005.0073 arXiv:0312002v1 [arXiv:q-bio]

Garanich, J.S., Pahakis, M., Tarbell, J.M.: Shear stress inhibits smooth muscle cell migration via nitric oxide-mediated downregulation of matrix metalloproteinase-2 activity. American Journal of Physiology - Heart and Circulatory Physiology **288**(5

57-5), 2244–2252 (2005) https://doi.org/10.1152/ajpheart.00428.2003

Hao, W., Friedman, A.: The LDL-HDL profile determines the risk of atherosclerosis: A mathematical model. PLoS ONE **9**(3) (2014) https://doi.org/10.1371/journal.pone.0090497

Hsieh, H.J., Li, N.Q., Frangos, J.A.: Shear stress increases endothelial platelet-derived growth factor mRNA levels. American Journal of Physiology - Heart and Circulatory Physiology **260**(2 29-2), 1–5 (1991) https://doi.org/10.1152/ajpheart.1991.260.2.h642

Jaxa-Rozen, M., Kwakkel, J.H.: PyNetLogo: Linking NetLogo with Python. Journal of Artificial Societies and Social Simulation **21**(2) (2018) https://doi.org/10.18564/jasss.3668

Kona, S., Chellamuthu, P., Xu, H., Hills, S.R., Nguyen, K.T.: Effects of Cyclic Strain and Growth Factors on Vascular Smooth Muscle Cell Responses. The Open Biomedical Engineering Journal **3**(1), 28–38 (2009) https://doi.org/10.2174/1874120700903010028

Koyama, N., Hart, C.E., Clowes, A.W.: Different functions of the platelet-derived growth factor-α and -β receptors for the migration and proliferation of cultured baboon smooth muscle cells. Circulation Research **75**(4), 682–691 (1994) https://doi.org/10.1161/01.RES.75.4.682

Keshavarzian, M., Meyer, C.A., Hayenga, H.N.: Mechanobiological model of arterial growth and remodeling. Biomechanics and Modeling in Mechanobiology **17**(1), 87–101 (2018) https://doi.org/10.1007/s10237-017-0946-y

Keshavarzian, M., Meyer, C.A., Hayenga, H.N.: In Silico Tissue Engineering: A Coupled Agent-Based Finite Element Approach. Tissue Engineering - Part C: Methods **25**(11), 641–654 (2019) https://doi.org/10.1089/ten.tec.2019.0103

Krick, S., Platoshyn, O., Sweeney, M., McDaniel, S.S., Zhang, S., Rubin, L.J., Yuan, J.X.J.: Nitric oxide induces apoptosis by activating K+ channels in pulmonary vascular smooth muscle cells. American Journal of Physiology - Heart and Circulatory Physiology **282**(1 51-1), 184–193 (2002) https://doi.org/10.1152/ajpheart.2002.282.1.h184

Li, S., Lei, L., Hu, Y., Zhang, Y., Zhao, S., Zhang, J.: A fully coupled framework for in silico investigation of in-stent restenosis. Computer Methods in Biomechanics and Biomedical Engineering **22**(2), 217–228 (2019) https://doi.org/10.1080/10255842.2018.1545017

Minion, D.J., Snajdar, R.M., Van De Kerkhove, M.P., Van Aalst, J.A., Fox, P.L., Graham, L.M.: The migratory response to platelet-derived growth factor of smooth muscle cells isolated from synthetic vascular grafts in a canine model. Journal of

Vascular Surgery **31**(5), 953–959 (2000) https://doi.org/10.1067/mva.2000.106419

Nerem, R.M., Alexander, R.W., Chappell, D.C., Medford, R.M., Varner, S.E., Robert Taylor, W.: The Study of the Influence of Flow on Vascular Endothelial Biology. The American Journal of the Medical Sciences **316**(3), 169–175 (1998) https://doi.org/10.1016/s0002-9629(15)40397-0

Noble, C., Carlson, K.D., Neumann, E., Dragomir-Daescu, D., Erdemir, A., Lerman, A., Young, M.: Patient specific characterization of artery and plaque material properties in peripheral artery disease. Journal of the Mechanical Behavior of Biomedical Materials **101**, 103453 (2020) https://doi.org/10.1016/j.jmbbm.2019.103453

Nolan, D.R., Lally, C.: An investigation of damage mechanisms in mechanobiological models of in-stent restenosis. Journal of Computational Science **24**, 132–142 (2018) https://doi.org/10.1016/j.jocs.2017.04.009

Noël, C.: A three-dimensional visco-hyperelastic FE model for simulating the mechanical dynamic response of preloaded phalanges. Medical Engineering and Physics **61**, 41–50 (2018) https://doi.org/10.1016/j.medengphy.2018.08.007

Noől, C., Settembre, N.: Assessing mechanical vibration-altered wall shear stress in digital arteries. Journal of Biomechanics **131**, 110893 (2022) https://doi.org/10.1016/j.jbiomech.2021.110893

Noël, C., Settembre, N.: Near-wall hemodynamic parameters of finger arteries altered by hand-transmitted vibration. Computers in Biology and Medicine **168**, 107709 (2024) https://doi.org/10.1016/j.compbiomed.2023.107709

Ohno, M., Cooke, J.P., Dzau, V.J., Gibbons, G.H.: Fluid Shear Stress Induces Endothelial Transforming Growth Factor Beta-1 Transcription and Production: Modulation by Potassium Channel Blockade. Journal of Clinical Investigation **95**(3), 1363–1369 (1995) https://doi.org/10.1172/JCI117787

Okada, A., Inaba, R., Furuno, T.: Occurrence of intimal thickening of the peripheral arteries in response to local vibration. British Journal of Industrial Medicine **44**(7), 470–475 (1987) https://doi.org/10.1136/oem.44.7.470

Panwar, P., Butler, G.S., Jamroz, A., Azizi, P., Overall, C.M., Brömme, D.: Aging-associated modifications of collagen affect its degradation by matrix metalloproteinases. Matrix Biology **65**, 30–44 (2018) https://doi.org/10.1016/j.matbio.2017.06.004

Reda, M., Noel, C., Settembre, N., Chambert, J., Lejeune, A., Jacquet, E.: Agent-based modelling of the smooth muscle cells migration induced by mechanical vibration : a preliminary study. Computer Methods in Biomechanics and Biomedical Engineering **23**(S1), 255–256 (2020) https://doi.org/10.1080/10255842.2020.1815326

Reda, M., Noël, C., Settembre, N., Chambert, J., Lejeune, A., Rolin, G., Jacquet, E.: An agent-based model of vibration-induced intimal hyperplasia. Biomechanics and Modeling in Mechanobiology **21**(5), 1457–1481 (2022) https://doi.org/10.1007/s10237-022-01601-5

Stoyneva, Z., Lyapina, M., Tzvetkov, D., Vodenicharov, E.: Current pathophysiological views on vibration-induced Raynaud's phenomenon. Cardiovascular Research **57**(3), 615–624 (2003) https://doi.org/10.1016/S0008-6363(02)00728-9

Sakamoto, N., Ohashi, T., Sato, M.: Effect of fluid shear stress on migration of vascular smooth muscle cells in cocultured model. Annals of Biomedical Engineering **34**(3), 408–415 (2006) https://doi.org/10.1007/s10439-005-9043-y

Schiavone, A., Zhao, L.G.: A study of balloon type, system constraint and artery constitutive model used in finite element simulation of stent deployment. Mechanics of Advanced Materials and Modern Processes **1**(1), 1–15 (2015) https://doi.org/10.1186/s40759-014-0002-x

Takeuchi, T., Futatsuka, M., Imanishi, H., Yamada, S.: Pathological changes observed in the finger biopsy of patients with vibration-induced white finger. The Scandinavian Journal of Work, Environment and Health **12**, 280–283 (1985)

Tahir, H., Hoekstra, A.G., Lorenz, E., Lawford, P.V., Rodney Hose, D., Gunn, J., Evans, D.J.W.: Multi-scale simulations of the dynamics of in-stent restenosis: Impact of stent deployment and design. Interface Focus **1**(3), 365–373 (2011) https://doi.org/10.1098/rsfs.2010.0024

Wilensky, U., Hazzard, E., Froemke, R.: GasLab: an extensible modeling toolkit for exploring statistical mechanics. In: Seventh European Logo Conference (EUROLOGO '99), Sofia, Bulgaria (1999). https://ccl.northwestern.edu

Wriggers, P.: Nonlinear Finite Element Methods. Springer, Berlin, Heidelberg (2008). https://doi.org/10.1007/978-3-540-71001-1

Wolf, S.C., Sauter, G., Rodemann, H.P., Risler, T., Brehm, B.R.: Influence of growth factors on the proliferation of vascular smooth muscle cells isolated from subtotally nephrectomized rats after endothelin or angiotensin II antagonism. Nephrology Dialysis Transplantation **20**(2), 312–318 (2005) https://doi.org/10.1093/ndt/gfh606

Wang, W., Zhao, T., Geng, K., Yuan, G., Chen, Y., Xu, Y.: Smoking and the Pathophysiology of Peripheral Artery Disease. Frontiers in Cardiovascular Medicine **8**(August), 1–17 (2021) https://doi.org/10.3389/fcvm.2021.704106

Zahedmanesh, H., Lally, C.: A multiscale mechanobiological modelling framework using agent-based models and finite element analysis: Application to vascular tissue engineering. Biomechanics and Modeling in Mechanobiology **11**(3-4), 363–377 (2012) https://doi.org/10.1007/s10237-011-0316-0

Appendix A ABM rules

Appendix A summarizes the parameters used in the mechanobiological framework. For each parameter, the corresponding value, unit and associated references are provided.

Table A1 WSS-dependent factors secretion.

Parameter	Equation	Graphs and References
Mass production rate of PDGF-BB by one EC (EC-secreted) $\dot{\boldsymbol{m}}^{\mathbf{EC}}_{\mathbf{PDGF-BB}}(\boldsymbol{\tau})$ [fg·s^{-1}]	$\dot{\boldsymbol{m}}^{\mathbf{EC}}_{\mathbf{PDGF-BB}}(\boldsymbol{\tau}) = \alpha Q^1_{\text{PDGF-BB}}(1-\exp(-(\tau-\tau_{\text{phys}})/\kappa^1_{\text{PDGF-BB}})) + Q^2_{\text{PDGF-BB}}(1-\exp((\tau-\tau_{\text{phys}})/\kappa^2_{\text{PDGF-BB}})) + q_{\text{PDGF-BB}}(\tau-\tau_{\text{phys}})$ $\tau_{\text{phys}} = 3$ Pa **if $0.6 \leq \tau \leq 3$ Pa**: $\alpha = -1$, $Q^1_{\text{PDGF-BB}} = 5.44\times10^{-5}$ fg·s^{-1}, $\kappa^1_{\text{PDGF-BB}} = 1$ Pa, $Q^2_{\text{PDGF-BB}} = 5.15\times10^{-4}$ fg·s^{-1}, $\kappa^2_{\text{PDGF-BB}} = 1$ Pa, $q_{\text{PDGF-BB}} = 2.94\times10^{-4}$ fg·s^{-1}·Pa^{-1} **if $\tau \geq 3$ Pa**: $\alpha = 1$, $Q^1_{\text{PDGF-BB}} = 2.54\times10^{-4}$ fg·s^{-1}, $\kappa^1_{\text{PDGF-BB}} = 0.6746$ Pa, $Q^2_{\text{PDGF-BB}} = 0$ fg·s^{-1}, $\kappa^2_{\text{PDGF-BB}} = 1$ Pa, $q_{\text{PDGF-BB}} = 0$ fg·s^{-1}·Pa^{-1}	Hsieh et al. (1991), Experimental measurements (Reda e
Mass production rate of TGF-β by one EC (EC-secreted) $\dot{\boldsymbol{m}}^{\mathbf{EC}}_{\mathbf{TGF-}\boldsymbol{\beta}}(\boldsymbol{\tau})$ [fg·s^{-1}]	$\dot{\boldsymbol{m}}^{\mathbf{EC}}_{\mathbf{TGF-}\boldsymbol{\beta}}(\boldsymbol{\tau}) = Q_{\text{TGF-}\beta} + q_{\text{TGF-}\beta}\times\tau$ $Q_{\text{TGF-}\beta} = 4.26\times10^{-4}$ fg·s^{-1} $q_{\text{TGF-}\beta} = 4.26\times10^{-4}$ fg·s^{-1}·Pa^{-1}	Ohno et al. (1995), Cucina et al. (1998)
NO molar concentration (EC-secreted) $\boldsymbol{C}^{\mathbf{EC}}_{\mathbf{NO}}(\boldsymbol{\tau})$ [nM]	$\boldsymbol{C}^{\mathbf{EC}}_{\mathbf{NO}}(\boldsymbol{\tau}) = C_1(1-\exp(-\tau/\kappa_{\text{NO}})) + C_2$ $C_1 = 51.7\times T$ [nM], $\kappa_{\text{NO}} = 0.95$ Pa $C_2 = 20.22\times T$ [nM] T [hours]	Andrews et al. (2010)
Mass of MMP-2 by one SMC $\boldsymbol{m}^{\mathbf{SMC}}_{\mathbf{MMP-2}}(\boldsymbol{\tau})$ [fg]	$\boldsymbol{m}^{\mathbf{SMC}}_{\mathbf{MMP-2}}(\boldsymbol{\tau}) = M^1_{\text{MMP-2}}(\exp(-(\tau-\tau_{\text{phys}})/\kappa^1_{\text{MMP-2}})-1)$ $\tau_{\text{phys}} = 3$ Pa $M^1_{\text{MMP-2}} = 2.656\times10^{-5}\times T$ [fg] $\kappa^1_{\text{MMP-2}} = 1$ Pa T [hours]	Sakamoto et al. (2006), Garanich et al. (2005)

Table A2 Stress-dependent factors secretion.

Parameter	Equation	References
Mass of PDGF-BB secreted by one SMC (SMC-secreted) $\boldsymbol{m^{SMC}_{PDGF-BB}(\sigma_\theta)}$ [fg]	**if** $\boldsymbol{\sigma_\theta \geq \sigma_{max}}$: $\boldsymbol{m^{SMC}_{PDGF-BB}(\sigma_\theta)} = m_{PDGF-BB} \times \sigma_\theta - M_{PDGF-BB}$ $m_{PDGF-BB} = 7.98 \times 10^{-5} \times T$ [fg·kPa^{-1}], $M_{PDGF-BB} = 5.4264 \times 10^{-3} \times T$ [fg] T [hours]	Keshavarzian et al. (2018), Bayer et al. (1999)
Correcting factor for PDGF-BB $\boldsymbol{C_f(\sigma_\theta)}$ [-]	**if PDGF-BB (EC-secreted) > 0 and** $\boldsymbol{\sigma_\theta \leq \sigma_{min}}$: $\boldsymbol{C_f(\sigma_\theta)} = \beta^1_{PDGF-BB} \times \sigma_\theta + \beta^2_{PDGF-BB}$ $\beta^1_{PDGF-BB} = 7.98 \times 10^{-5} \times T$ [kPa^{-1}], $\beta^2_{PDGF-BB} = -3.99 \times 10^{-3} \times T$ [-] T [hours]	
Mass of TGF-β secreted by one SMC (SMC-secreted) $\boldsymbol{m^{SMC}_{TGF-\beta}(\sigma_\theta)}$ [fg]	**if** $\boldsymbol{\sigma_\theta \geq \sigma_{max}}$ $\boldsymbol{m^{SMC}_{TGF-\beta}(\sigma_\theta)} = m_{TGF-\beta} \times \sigma_\theta - M_{TGF-\beta}$ $m_{TGF-\beta} = 2.76 \times 10^{-4} \times T$ [fg·kPa^{-1}], $M_{TGF-\beta} = 1.8768 \times 10^{-2} \times T$ [fg] T [hours]	Keshavarzian et al. (2018)
Mass of MMP-2 secreted by one SMC $\boldsymbol{m^{SMC}_{MMP-2}(\sigma_\theta)}$ [fg]	$\boldsymbol{m^{SMC}_{MMP-2}(\sigma_\theta)} = M^2_{MMP-2}(1 - \exp(\alpha((\sigma_\theta - \sigma^{phys}_\theta)/\kappa^2_{MMP-2})))$ **if** $\boldsymbol{\sigma_\theta \geq \sigma_{max}}$: $\alpha = -1$ $\sigma^{phys}_\theta = \sigma_{max}$: $M^2_{MMP-2} = 7.347 \times 10^{-2} \times T$ [fg] , $\kappa^2_{MMP-2} = 56.28$ kPa T [hours] **if** $\boldsymbol{\sigma_\theta \leq \sigma_{min}}$: $\alpha = 1$ $\sigma^{phys}_\theta = \sigma_{min}$: $M^2_{MMP-2} = 8.67 \times 10^{-2} \times T$ [fg] , $\kappa^2_{MMP-2} = 56.28$ kPa T [hours]	Keshavarzian et al. (2018) Bayer et al. (1999)
Mass of MMP-9 secreted by one SMC $\boldsymbol{m^{SMC}_{MMP-9}(\sigma_\theta)}$ [fg]	**if** $\boldsymbol{\sigma_\theta \geq \sigma_{max}}$: $\boldsymbol{m^{SMC}_{MMP-9}(\sigma_\theta)} = M_{MMP-9}(1 - \exp(-((\sigma_\theta - \sigma^{phys}_\theta)/\kappa_{MMP-9})))$ $\sigma^{phys}_\theta = \sigma_{max}$ $M_{MMP-9} = 2.118 \times 10^{-4} \times T$ [fg] , $\kappa_{MMP-9} = 26$ kPa T [hours]	Keshavarzian et al. (2018)

Table A3 SMC dynamics implemented in the ABM.

Event	Equation	Graphs and References
SMCs proliferation probability for one SMC in one T $\boldsymbol{\mathcal{P}}$ [-]	$\boldsymbol{\mathcal{P}} = \mathcal{P}_{\text{basal}} + \mathcal{P}_{\text{PDGF-BB}} + \mathcal{P}_{\text{TGF-}\beta}$ $\boldsymbol{\mathcal{P}_{\text{basal}}} = 1.46 \times 10^{-4}$ $\boldsymbol{\mathcal{P}_{\text{PDGF-BB}}} = A^1_{\text{PDGF-BB}}(1 - \exp(-m_{\text{PDGF-BB}}/\omega^1_{\text{PDGF-BB}}))$ $+\alpha A^2_{\text{PDGF-BB}} \times m_{\text{PDGF-BB}}$ $A^1_{\text{PDGF-BB}} = 2.323 \times 10^{-2}$ $m_{\text{PDGF-BB}} = m^{\text{SMC}}_{\text{PDGF-BB}} + m^{\text{EC}}_{\text{PDGF-BB}}$ (from diffusion) $+ C_f \times m_{\text{unit}}$ [fg], $\omega^1_{\text{PDGF-BB}} = 4.33$ fg $\alpha = -1$ $A^2_{\text{PDGF-BB}} = 3.35 \times 10^{-6}$ $m_{\text{unit}} = 1$ fg $\boldsymbol{\mathcal{P}_{\text{TGF-}\beta}} = A_{\text{TGF-}\beta} \exp(-m_{\text{TGF-}\beta}/\omega_{\text{TGF-}\beta})$, $A_{\text{TGF-}\beta} = 2.936 \times 10^{-4}$, $m_{\text{TGF-}\beta} = m^{\text{SMC}}_{\text{TGF-}\beta} + m^{\text{EC}}_{\text{TGF-}\beta}$ (from diffusion) [fg] $\omega_{\text{TGF-}\beta} = 10^{-3}$ fg	Wolf et al. (2005), Cucina et al. (1998)
SMCs apoptosis probability for one SMC in one T $\boldsymbol{\mathcal{A}}$ [-]	$\boldsymbol{\mathcal{A}} = \mathcal{A}_{\text{basal}} + \mathcal{A}_{\text{NO}}$ $\boldsymbol{\mathcal{A}_{\text{basal}}} = 1.46 \times 10^{-4}$ $\boldsymbol{\mathcal{A}_{\text{NO}}} = \gamma_{\text{NO}} \times (C^{\text{EC}}_{\text{NO}} - {}^{\text{phys}}C^{\text{EC}}_{\text{NO}})$ $\gamma_{\text{NO}} = 7.317 \times 10^{-7}$ nM^{-1} ${}^{\text{phys}}C^{\text{EC}}_{\text{NO}} = 69.7$ nM	Krick et al. (2002)
SMCs migration probability for one SMC in one T $\boldsymbol{\mathcal{M}}$ [-]	$\boldsymbol{\mathcal{M}} = A_{\text{PDGF-BB}}(1 - \exp(-m^{\text{EC}}_{\text{PDGF-BB}}/\omega_{\text{PDGF-BB}}))$ $A_{\text{PDGF-BB}} = 7.913 \times 10^{-4}$, $m^{\text{EC}}_{\text{PDGF-BB}}$ (from diffusion) [fg] $\omega_{\text{PDGF-BB}} = 4.9 \times 10^{-2}$ fg	Dardik et al. (2005), Bornfeldt et al. (1994)

Table A4 ECM dynamics implemented in the ABM.

Event	Equation	Graphs and References
Collagen synthesis probability in media for one SMC in one T $\boldsymbol{\mathcal{S}^{\mathrm{m}}}$ [-]	$\boldsymbol{\mathcal{S}^{\mathrm{m}}} = \mathcal{S}^{\mathrm{m}}_{\mathrm{basal}} + \mathcal{S}^{\mathrm{m}}_{\mathrm{TGF-}\beta}$ $\boldsymbol{\mathcal{S}^{\mathrm{m}}_{\mathrm{basal}}} = 1.07 \times 10^{-5}$ $\boldsymbol{\mathcal{S}^{\mathrm{m}}_{\mathrm{TGF-}\beta}} = \gamma_{\mathrm{TGF-}\beta} \times m^{\mathrm{SMC}}_{\mathrm{TGF-}\beta}$ $\gamma_{\mathrm{TGF-}\beta} = 2.27 \times 10^{-5}$ fg^{-1} $m^{\mathrm{SMC}}_{\mathrm{TGF-}\beta}$ [fg]	Keshavarzian et al. (2018), Zahedmanesh and Lally (2012)
Collagen synthesis probability in intima for one SMC in one T $\boldsymbol{\mathcal{S}^{\mathrm{i}}}$ [-]	$\boldsymbol{\mathcal{S}^{\mathrm{i}}} = \mathcal{S}^{\mathrm{i}}_{\mathrm{basal}} + \mathcal{S}^{\mathrm{i}}_{\mathrm{TGF-}\beta}$ $\boldsymbol{\mathcal{S}^{\mathrm{i}}_{\mathrm{basal}}} = 2.24 \times 10^{-5}$ $\mathcal{S}^{\mathrm{i}}_{\mathrm{TGF-}\beta} = \mathcal{S}^{\mathrm{m}}_{\mathrm{TGF-}\beta}$	Okada et al. (1987)
Collagen degradation probability for one SMC in one T $\boldsymbol{\mathcal{D}^{\mathrm{c}}}$ [-]	$\boldsymbol{\mathcal{D}^{\mathrm{c}}} = \mathcal{D}^{\mathrm{c}}_{\mathrm{basal}} + \mathcal{D}^{\mathrm{c}}_{\mathrm{MMP-2}}$ $\boldsymbol{\mathcal{D}^{\mathrm{c}}_{\mathrm{basal}}} = 1.07 \times 10^{-5}$ $\boldsymbol{\mathcal{D}^{\mathrm{c}}_{\mathrm{MMP-2}}} = \gamma^{1}_{\mathrm{MMP-2}} \times m_{\mathrm{MMP-2}}$ $\gamma^{1}_{\mathrm{MMP-2}} = 3.5 \times 10^{-4}$ fg^{-1} $m_{\mathrm{MMP-2}} = m^{\mathrm{SMC}}_{\mathrm{MMP-2}}(\tau) + m^{\mathrm{SMC}}_{\mathrm{MMP-2}}(\sigma_\theta)$[fg]	Zahedmanesh and Lally (2012)
Elastin degradation probability for one SMC in one T $\boldsymbol{D^{\mathrm{e}}}$ [-]	$\boldsymbol{\mathcal{D}^{\mathrm{e}}} = \mathcal{D}^{\mathrm{e}}_{\mathrm{MMP-2}} + \mathcal{D}^{\mathrm{e}}_{\mathrm{MMP-9}}$ $\boldsymbol{\mathcal{D}^{\mathrm{e}}_{\mathrm{MMP-2}}} = \gamma^{2}_{\mathrm{MMP-2}} \times m_{\mathrm{MMP-2}}$ $\boldsymbol{\mathcal{D}^{\mathrm{e}}_{\mathrm{MMP-9}}} = \gamma_{\mathrm{MMP-9}} \times m_{\mathrm{MMP-9}}$ $\gamma^{2}_{\mathrm{MMP-2}} = 3.1429 \times 10^{-6}$ fg^{-1} $\gamma_{\mathrm{MMP-9}} = 1.036 \times 10^{-6}$ fg^{-1} $m_{\mathrm{MMP-2}} = m^{\mathrm{SMC}}_{\mathrm{MMP-2}}(\tau) + m^{\mathrm{SMC}}_{\mathrm{MMP-2}}(\sigma_\theta)$[fg] $m_{\mathrm{MMP-9}} = m^{\mathrm{SMC}}_{\mathrm{MMP-9}}(\sigma_\theta)$ [fg]	Zahedmanesh and Lally (2012)
MMP-2 removal in time T	1% MMP-2	Zahedmanesh and Lally (2012)
MMP-9 removal in time T	MMP-9 / 2.11	Keshavarzian et al. (2018)